Experimentally Based Modeling of Field Sources for Three-Dimensional Computation of SAR in Electromagnetic Hyperthermia and Treatment Planning

Mikaya L. D. Lumöri, *Member, IEEE*

***Abstract*—This paper presents field source-modeling, for applications to hyperthermia, by utilizing experimental data from the paraxial region of a liquid muscle-like phantom irradiated by an aperture antenna. The data are used in an optimization algorithm, applied to a Gaussian beam model (GBM), to determine the source parameters for GBM-computations of specific absorption rates everywhere, accurate to within 1% (relative to the global maximum) of the experimental results. This paper also shows how the aperture and incident fields may be determined accurately by the GBM and links them to the electric-field integral equation (EFIE), as an example, to improve the accuracy of numerical computations of the electric or magnetic fields associated with the EFIE, the magnetic-field integral equation, or any other field formulations. It is further demonstrated that models of plane waves, or approximate source fields, predict power levels with significant, unacceptable errors. Finally, it is concluded that the GBM is a viable tool for characterizing aperture antennas used in hyperthermia for cancer therapy.**

I. Introduction

THERE ARE several types of electromagnetic radiating antennas used for localized or regional hyperthermic treatment of tumors. These are based on waveguiding structures, operating at a frequency in the range 100–2000 MHz. Examples are horn antennas consisting of hollow, open-ended waveguides with rectangular or circular cross sections or microstrip antennas which are patches or spirals. These may be used individually or as phased arrays for superficial or deep hyperthermia, but their performance must be ascertained by application of three-dimensinal (3-D) numerical models to the *electric field integral-equation* (EFIE), the *magnetic field integral-equation* (MFIE), etc., to simulate SAR in a tumor. Improvement of SAR simulations is possible if the field sources are modeled accurately. To this end, this paper presents accurate source modeling by use of the Gaussian beam model (GBM) [1].

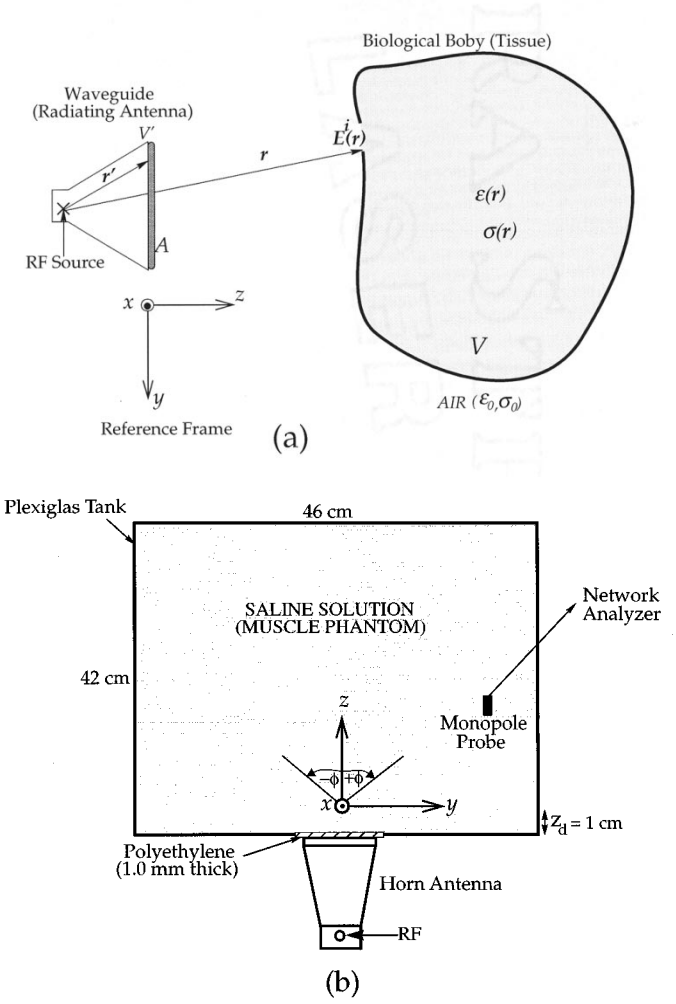

Fig. 1. (a) Reference frame of a biological body subjected to microwave irradiation from an aperture (A) antenna source and (b) liquid muscle-like phantom field scan set-up ($\sigma = 1.09$ S/m, $\varepsilon_r = 77.14$ at 400 MHz and $\sigma = 1.2$ S/m, $\varepsilon_r = 56$ at 450 MHz).

Manuscript received April 23, 1999. This work was supported and facilities provided by Prof. A. Barel, Chairman, Department of Electrical Engineering, Vrije Universiteit, Brussels, Belgium.

The author was with the Department of Electrical Engineering, Vrije Universiteit Brussel, B-1050 Brussels, Belgium. He is now with the Department of Engineering, University of San Diego, San Diego, CA 92110 USA.

Publisher Item Identifier S 0018-9480(00)07396-8.

Consider, for example, the EFIE formulated for the total electric field, $\boldsymbol{E}(\boldsymbol{r})$, induced in a biological body of volume V [2], in Fig. 1(a), typically implemented by the MOM, *viz*

$$[\tilde{\boldsymbol{G}}][\boldsymbol{E}] = -[\boldsymbol{E}^{\boldsymbol{i}}] \tag{1}$$

where

$[\tilde{G}]$ dyadic Green's function matrix;
$[E]$ total electric field matrix;
$[E^i]$ matrix of the incident field, derived from a known aperture field, $E(r')$.

Conventionally, if the problem is sufficiently known, the aperture field is modeled by *Huygens' sources* in free space for plane waves [3]. In hyperthermia, however, RF sources that do not necessarily engender plane waves are used [4]. Besides, the aperture field changes due to irregularities (water-bolus, etc.) in the vicinity of the lossy body (target), making it difficult to define the problem.

In an effort to improve source-field modeling, some analytical methods for focused power were published [5]–[8] and verified experimentally [9], [10]. A method based on Gaussian beams to model the field sources accurately is presented in this paper. After all, Gaussian beams have been used in lossless media as models of local electromagnetic fields in the design of microwave systems [11]–[16]. Also, superposition Gaussian beams have been used for modeling transient ultrasonic waves [17], source fields [18], and in the identification of parametric wave propagation models for ultrasonic transmission experiments [19].

In general, however, Gaussian beams cannot be used to model fields from an aperture antenna because the aperture field distributions are not Gaussian; but investigations have shown that when the aperture is close to a lossy medium its field distribution is fairly smooth in the lossy medium and is well represented by a local Gaussian curve, in amplitude and phase [10], [20]. Thus the limitations found in free space are eliminated because the high spatial frequencies are damped out, leaving a smooth curve.

II. The GBM and the EFIE

A. GBM Formulation

The field sources may be modeled by the fundamental astigmatic Gaussian beam, outlined below for a homogeneous medium of infinite size [1], [10]. Neglecting polarization effects, we pull out the dominant axial term $U(x, y, z) = \Psi(x, y, z)e^{-jkz}$ from the wave equation $(\nabla^2 + k^2)U(x, y, z) = 0$. The differential equation for $\Psi(x, y, z)$, a slowly varying function, is

$$\frac{\partial^2\Psi}{\partial x^2} + \frac{\partial^2\Psi}{\partial y^2} - 2jk\frac{\partial\Psi}{\partial z} + \frac{\partial^2\Psi}{\partial z^2} = 0$$

where $k = \omega(\mu\varepsilon')^{1/2} = \beta - j\alpha$ is the wave propagation constant, with β and α the respective phase and attenuation constants. Invoking the usual high-frequency asymptotic approximation, where the second-order axial derivative is negligible, we attain the parabolic equation. The following astigmatic beam expression is an exact solution to the parabolic equation [10], [11]:

$$E(x, y, z) = \frac{E_0 e^{-jkz}}{\sqrt{(z-a)(z-b)}} \cdot e^{[(-jkx^2)/(2(z-a))]} e^{[(-jky^2)/(2(z-b))]}. \quad (2)$$

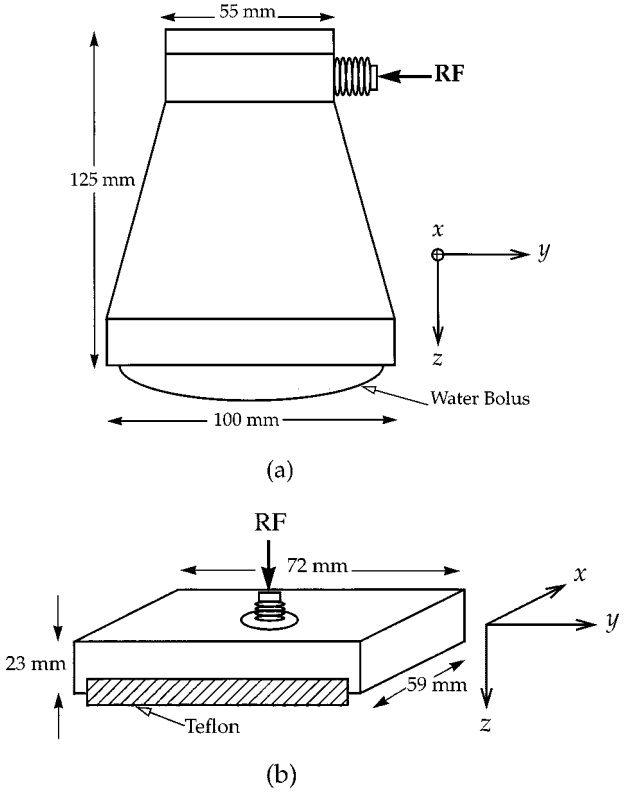

Fig. 2. Schematics of (a) SMA (Italian Company) multifrequency water-loaded waveguide applicator with a circular aperture and (b) current sheet applicator (CSA) inductive microwave aperture antenna with a teflon aperture for interface matching.

This is the GBM where $a = a_1 + ja_2$ and $b = b_1 + jb_2$ are arbitrary complex source parameters in the principal E- and H-planes, respectively (a_1, a_2, b_1, and b_2 are real spatial values), with E_0 a constant. The source parameters may vary slightly with frequency but are unique for each aperture antenna. When a and b are large, a plane wave ensues. However, finite values of a and b result in the proper transverse and axial decays. Literature on Gaussian beams in lossy media reveals how the complex sources define the waist for a focused system, the evolution of the waist, etc. [20].

This paper uses (2) by fitting experimental data and then letting the Gaussian beam describe the field everywhere else. When the beam meets a curved interface at normal incidence to a different medium, its parameters change in a simple way [1], [10], [16]. Plane wave reflection and transmission coefficients are used for the evaluation of amplitudes at interfaces of different media.

B. Application of the GBM

In a treatment planning setup, a water-bolus is placed between the aperture antenna and the body (muscle) for matching and cooling. The entire system must be modeled by measuring the aperture and incident fields in the liquid muscle-like phantom in Fig. 1(b). Any other method which precludes the fields in the aperture–bolus–air–muscle interfaces is apt to err.

1) The Geometrical (GEO_GBM) Method: Prerequisites for GBM application are field amplitude and phase measure-

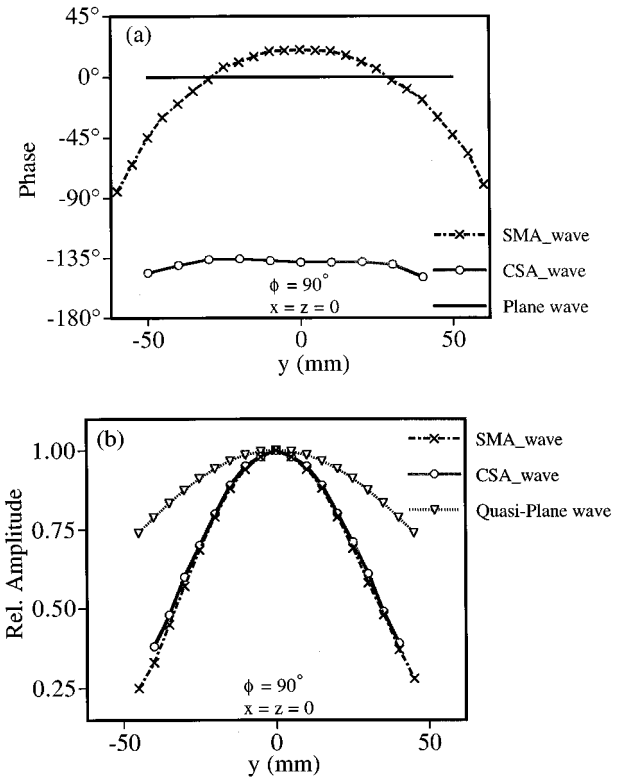

Fig. 3. Principal $\boldsymbol{E}$-plane experimental (SMA_wave & CSA_wave) and theoretical (plane- and quasi-plane-waves) results of (a) field phase and (b) relative field amplitude, close ($z_d = 1.0$ cm) to the apertures ($z = 0$ cm, reference) at $\phi = 90°$ in Fig. 1(b), at 400 MHz for the SMA and for the plane- and quasi-plane waves and at 450 MHz for the CSA.

ments in the principal $\boldsymbol{E}$- and $\boldsymbol{H}$-planes. These are obtained from two orthogonal linear scans close to the aperture horn antenna, shown in Fig. 1(b). The half-power-widths ($x_{1/2}$ and $y_{1/2}$) and the radii of phase fronts (R_x and R_y) are derived from the data and used in (3) to compute the source parameters [1], [10], *viz.*

$$a = \frac{(\beta u_x - \alpha v_x) - j\,(\alpha u_x + \beta v_x)}{u_x^2 + v_x^2}$$

and

$$b = \frac{(\beta u_y - \alpha v_y) - j\,(\alpha u_y + \beta v_y)}{u_y^2 + v_y^2} \tag{3}$$

where

$$u_x = \frac{-\beta}{R_x}, \quad u_y = \frac{-\beta}{R_y}, \quad v_x = \frac{\ln 2}{x_{1/2}^2}$$

and

$$v_y = \frac{\ln 2}{y_{1/2}^2}.$$

The derived parameters are used in (2) to simulate the aperture field and power distributions everywhere else. This method works well [1], [10], [21], but the following disadvantages are apparent.

- $x_{1/2}$, $y_{1/2}$, R_x and R_y are approximated by a cumbersome, trial-and-error procedure.
- The measured phase and amplitude of a field must be symmetrical and well defined.
- Measurements of both phase (unlike the optimization method) and amplitude are required.

2) The Optimization (OPT_GBM) Method: Equation (4) represents the normalized power, P^{num}, derived from (2)

$$P^{\text{num}} = \frac{Q_0 e^{-2\alpha z}}{\sqrt{(q_1^2 + q_2^2)}}\, e^{f(x,\,y,\,z)} = \frac{N}{D} \tag{4}$$

where, from (3)

$$f(x,\,y,\,z) = \left[\frac{-x^2\alpha(z-a_1) + a_2\beta}{2(z-a_1)^2 + a_2^2} + \frac{-y^2\alpha(z-b_1) + b_2\beta}{2(z-b_1)^2 + b_2^2}\right]$$
$$q_1 = (z-a_1)(z-b_1) - a_2 b_2$$
$$q_s = a_2(z-b_1) + b_2(z-a_1)$$

and

$$Q_0 = \sqrt{(a_1^2 + a_2^2)}\Big|_{z=z_d}$$

where z_d is a constant [Fig. 1(b)].

From (4) the Jacobian matrix of P^{num}, a function of the complex source parameters, is

$$\frac{\partial P^{\text{num}}}{\partial v_i} = \frac{\left(D\dfrac{\partial N}{\partial v_i} - N\dfrac{\partial D}{\partial v_i}\right)}{D^2} \tag{5}$$

with v_i the only unknown, real variables (a_1, a_2, b_1, b_2). Equation (5) is utilized in a *least-square-error optimization algorithm* [22]. Measured data of normalized power, P_N, at various paraxial points (x, y, z) together with an initial guess of the parametric values are used in the *optimization algorithm*. The computed optimal source parameters are consistent with the numerically computed power P^{num} such that $||P_N - P^{\text{num}}||^2 \to 0$. Since there are only four parameters to be determined, a minimum of four data measurements are required.

This is a new, faster, and more accurate method than the geometrical method. Its advantages include: 1) field measurements of amplitude or power only; 2) rapid parametric optimization; and 3) application to more complex radiating antennas.

C. GBM Relevance to the EFIE

The EFIE (used as an example) is linked to the GBM through the incident field $\boldsymbol{E}^{\boldsymbol{i}}(\boldsymbol{r})$ in Fig. 1(a), which is a reference frame for a horn antenna irradiating an arbitrary 3-D lossy, inhomogeneous biological body of volume V surrounded by an unbounded, homogeneous medium (e.g., air: permittivity $= \varepsilon_0$ F/m, permeability $= \mu_0$ H/m and conductivity $= 0$).

1) EFIE Formulation: In Fig. 1(a) the incident field $\boldsymbol{E}^{\boldsymbol{i}}(\boldsymbol{r})$ gives rise to the scattered field, $\boldsymbol{E}^{\boldsymbol{s}}(\boldsymbol{r})$, in the body, inducing a current $\boldsymbol{J}(\boldsymbol{r}) = \tau(\boldsymbol{r})\boldsymbol{E}(\boldsymbol{r})$, where $\tau(\boldsymbol{r}) = \sigma(\boldsymbol{r}) + j\omega(\varepsilon(\boldsymbol{r}) - \varepsilon_0)$ and the total field $\boldsymbol{E}(\boldsymbol{r}) = \boldsymbol{E}^{\boldsymbol{i}}(\boldsymbol{r}) + \boldsymbol{E}^{\boldsymbol{s}}(\boldsymbol{r})$. The scattered (absorbed) field is expressed as [2]

$$\boldsymbol{E}^{\boldsymbol{s}}(\boldsymbol{r}) = \int_V \boldsymbol{J}(\boldsymbol{r})\Sigma\bar{\boldsymbol{G}}(\boldsymbol{r},\,\boldsymbol{r}')\,dV' - \frac{\boldsymbol{J}(\boldsymbol{r})}{2j\omega\varepsilon_0} \tag{6}$$

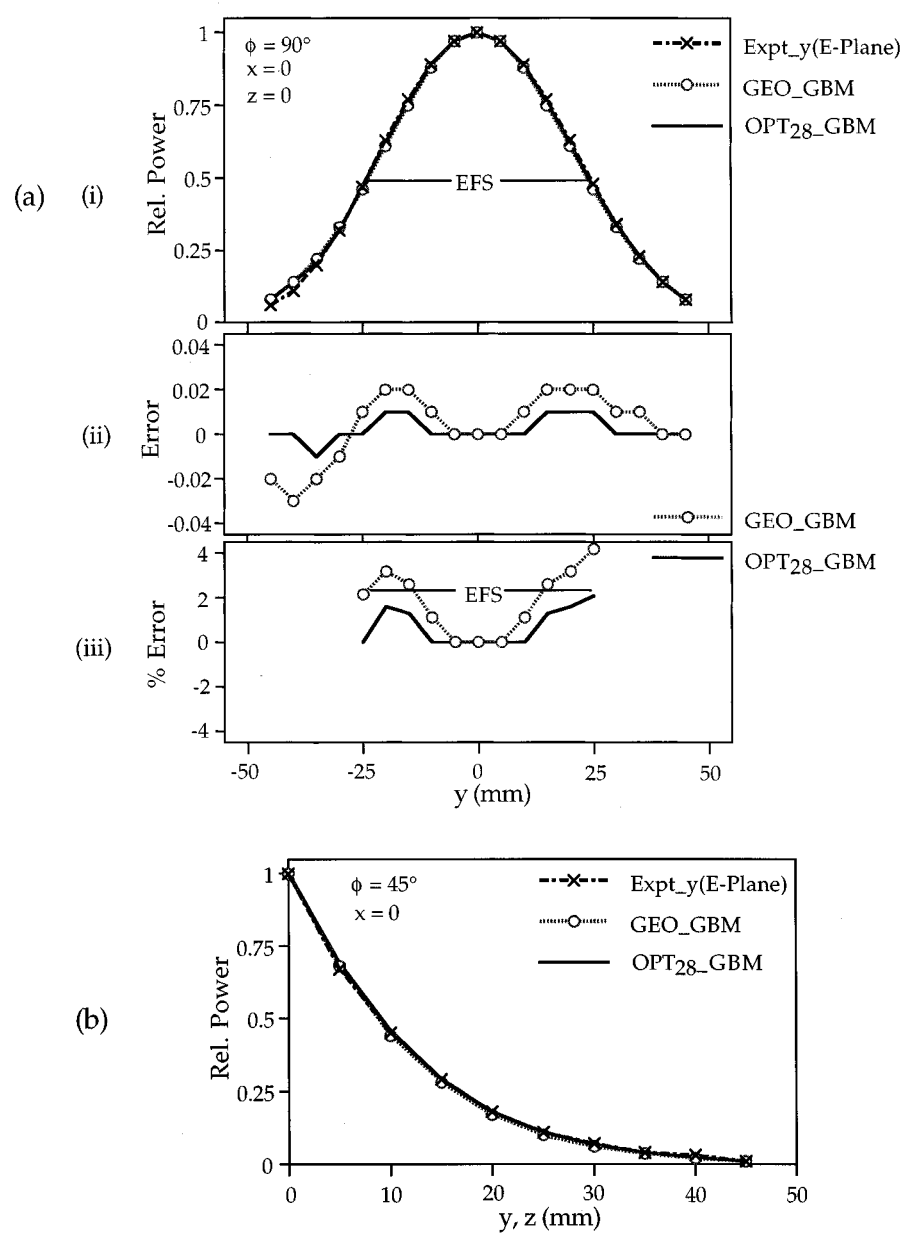

Fig. 4. SMA experimental [Expt_y(E-Plane)] and simulated (GEO_GBM & OPT28_GBM) results at 400 MHz in the principal $\boldsymbol{E}$-plane in Fig. 1(b) at: (a) $\phi = 90°$: (i) relative power, (ii) error (ref. global max.) and (iii) effective field size (EFS) % local error and (b) $\phi = 45°$.

where $\vec{\boldsymbol{G}}(\boldsymbol{r}, \boldsymbol{r}')$ is Green's dyadic function

$$\vec{\boldsymbol{G}}(\boldsymbol{r}, \boldsymbol{r}') = -j\omega\mu_0 \left[\bar{\boldsymbol{I}} + \frac{\nabla\nabla}{k_0^2}\right] \frac{e^{-jk_0|\boldsymbol{r}-\boldsymbol{r}'|}}{4\pi|\boldsymbol{r}-\boldsymbol{r}'|}$$

and

$$k_0 = \omega\sqrt{\mu_0\varepsilon_0}.$$

Equation (6) is the basic EFIE for the total electric field induced inside a biological body of volume V. Using the expressions above, it can easily be shown that

$$\int_V \tau(\boldsymbol{r}')\boldsymbol{E}(\boldsymbol{r}')\Sigma\vec{\boldsymbol{G}}(\boldsymbol{r}, \boldsymbol{r}')\, dV' - \left[1 + \frac{\tau(\boldsymbol{r})}{2j\omega\varepsilon_0}\right] \boldsymbol{E}(\boldsymbol{r}) = -\boldsymbol{E}^{\boldsymbol{i}}(\boldsymbol{r}) \tag{7a}$$

where

$$\boldsymbol{E}(\boldsymbol{r}) = \begin{bmatrix} E_x(\boldsymbol{r}) \\ E_y(\boldsymbol{r}) \\ E_z(\boldsymbol{r}) \end{bmatrix} \quad \boldsymbol{E}^{\boldsymbol{i}}(\boldsymbol{r}) = \begin{bmatrix} E_x^i(\boldsymbol{r}) \\ E_y^i(\boldsymbol{r}) \\ E_z^i(\boldsymbol{r}) \end{bmatrix}. \tag{7b}$$

Letting $x_1 = x$, $x_2 = y$ and $x_3 = z$ with $p, q = 1, 2, 3$, we obtain

$$\int_V \tau(\boldsymbol{r}') \left[\sum_{q=1}^{3} G_{x_p, x_q}(\boldsymbol{r}, \boldsymbol{r}') E_{x_q}(\boldsymbol{r}')\right] dV' - \left[1 + \frac{\tau(\boldsymbol{r})}{3j\omega\varepsilon_0}\right] E_{x_p}(\boldsymbol{r}) = -E_{x_p}^i(\boldsymbol{r}). \tag{8}$$

This is a linear operator to which the *method of moments* (MOM) is applied to obtain (1). Other numerical methods may be applied to the EFIE, or to other field formulations, but in each case the field sources must be accurately modeled to give a valid incident field.

2) Relevance of the GBM: If only $E_x^i(\boldsymbol{r})$ is excited in (7b), $E_y^i(\boldsymbol{r}) = E_z^i(\boldsymbol{r}) = 0$ and in Fig. 1(a) the two-dimensional (2-D) incident field is [23]

$$E_x^i(y, z) = 2\int_A \partial'_{\hat{a}_z} G_2(\overline{\rho}, \overline{\rho}')E_x(y', z')\,dy'\,dz' \qquad (9)$$

where $G_2(\overline{\rho}, \overline{\rho}') = -(j/4)H_0^{(2)}(k_0\rho)$ with $H_0^{(2)}(k_0\rho)$ the Hankel function of the second kind and zero order [3], A is the surface area of the *aperture*, $\rho = (y, z)$ is the tissue region, $\overline{\rho}' = (y', z')$ is aperture location, and $|\overline{\rho} - \overline{\rho}'| = \rho$. The validity of the incident field $E_x^i(y, z)$ depends on accurate modeling of the aperture field $E_x(y', z')$ and on the correct computation of (9).

In fact $E_x^i(y, z)$ and $E_x(y', z')$ are the 2-D versions of (2). Thus the GBM is linked to the EFIE with accurate aperture and incident fields which can be computed at low CPU times [1]. Moreover, the model copes very well with planar and curved boundaries of inhomogeneous layered media (e.g. bolus, skin, muscle, and fat), and is applicable to phased arrays [1], [10].

III. Methods, Results, and Discussion

A. Materials, Experimental Method, and Results

1) Materials: A liquid muscle-like phantom consisting of 6.65 g/l of a saline solution in water contained in a 42 cm × 46 cm Plexiglas tank 38 cm deep [Fig. 1(b)] was used in the experiment [1], [10]. The conductivity and relative permittivity of the phantom varied with frequency, saline concentration, and temperature [24].

A nonrectifying electric field probe was required to scan the E-field in the phantom. Oriented parallel to the dominant linearly polarized electric field, the probe consisted of a balanced dipole 10 mm long, 5 mm wide, formed by stripping a semirigid microcoaxial cable 1.5 mm in diameter [25]. To reduce field perturbations due to the metallic cable and errors from induced currents, the rest of the coaxial cable was oriented orthogonal to the E-field vector (z-direction). Also, the probe impedance was matched to the liquid muscle medium. A network analyzer (Hewlett Packard Model 8754A), used to process the phase and amplitude of the signal from the field probe, provided the RF signal.

2) Experimental Method: Two types of radiating aperture antenna (applicator) were used in the experiments: 1) a water-filled waveguide applicator [SMA (Italian Company)] [4], shown in Fig. 2(a) and 2) a current sheet applicator (CSA) in Fig. 2(b), a new type of applicator [21], [26]–[28]. The spatial distributions of the electric field were determined in the principal $\boldsymbol{E}$- and $\boldsymbol{H}$-planes of each applicator, at $z \geq z_d = 1.0$ cm from the aperture, by scanning the field probe under computer control through the liquid muscle-like phantom [1]. The measurements were processed in the network analyzer for phase, relative field and power data.

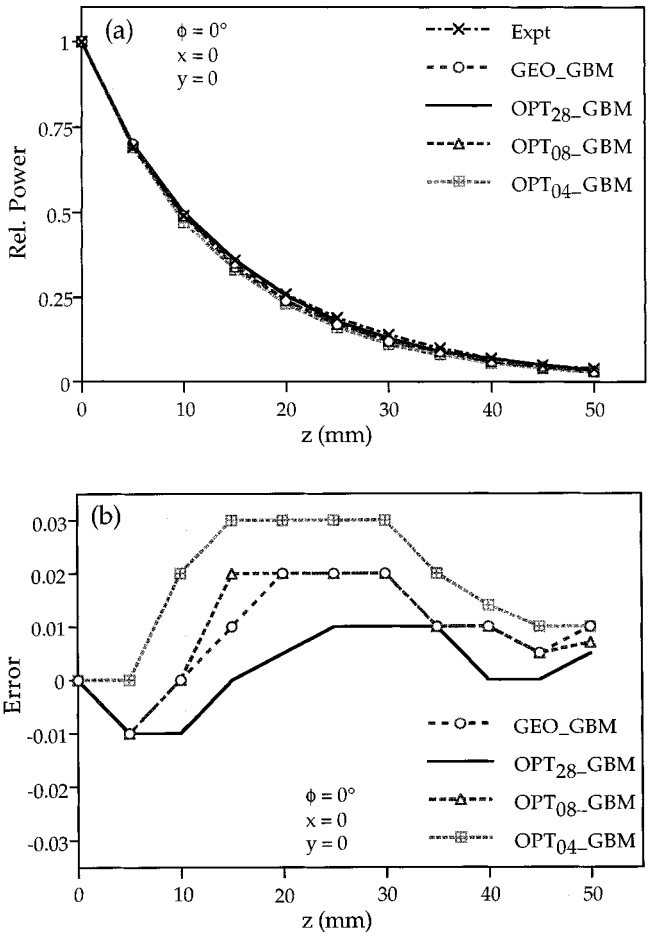

Fig. 5. SMA experimental (Expt) and simulated (GEO_GBM and OPT_GBM) results at 400 MHz in the principal $\boldsymbol{E}$- and $\boldsymbol{H}$-planes at $\phi = 0°$ in Fig. 1(b): (a) relative power and (b) error referenced to the global maximum (unity). [See Table I(A) for source parameters].

TABLE I
SMA Estimated Parameters and Rel. Power Errors

(A) ESTIMATED PARAMETRIC VALUES IN THE PRINCIPAL PLANES [$\boldsymbol{E}$-PLANE: $\mathbf{a = a_1 + ja_2}$ (cm); $\boldsymbol{H}$-PLANE: $\mathbf{b = b_1 + jb_2}$ (cm)]

PARAM (cm)	INITIAL (INI)	OPT_{04}_GBM (4 EXP DATA)	OPT_{08}_GBM (8 EXP DATA)	OPT_{28}_GBM (28 EXP DATA)	GEO_GBM* (PH.+AMPL.)
a_1	-1.0000	-1.6250	-3.1032	-2.8797	-2.7066*
a_2	-1.0000	-4.4190	-2.4184	-3.7072	-3.2681*
b_1	-1.0000	-3.7223	-3.7146	-3.8598	-3.7391*
b_2	-1.0000	-1.4055	-5.8040	-4.8411	-4.6112*

(B) EFS ABSOLUTE MAXIMAL RELATIVE POWER ERRORS (EXPERIMENT - SIMULATION)

SIMULATION METHOD	MAX. ERROR		MAX. % ERROR		ACCURACY (COMMENTS)
	$\boldsymbol{E}$- PLANE	$\boldsymbol{H}$-PLANE	$\boldsymbol{E}$- PLANE	$\boldsymbol{H}$-PLANE	
OPT_{04}_GBM	0.0103	0.0130	2.2%	2.5%	GOOD
OPT_{08}_GBM	0.0180	0.0033	3.8%	0.6%	GOOD
OPT_{28}_GBM	0.0105	0.0101	1.7%	1.9%	VERY GOOD
GEO_GBM	0.0220	0.0200	4.6%	3.8%	GOOD

3) Phase and Amplitude Results: These are shown in Fig. 3(a) together with a theoretical plane-wave phase, for comparison. For the SMA applicator the phase varies by over

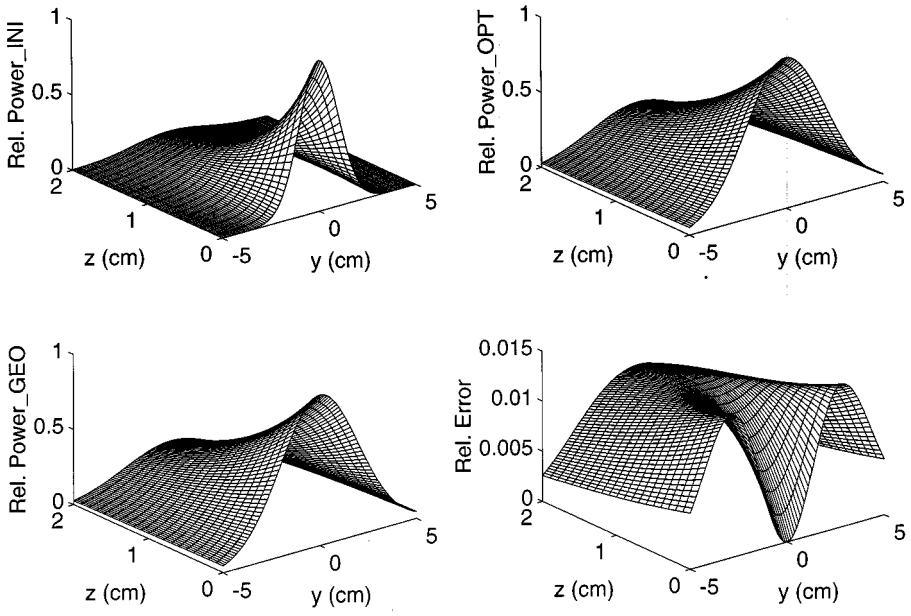

Fig. 6. SMA simulations at 400 MHz for (a) initial parameters: $a_1 = a_2 = b_1 = b_2 = -0.1000$ **cm**, (b) optimized parameters (OPT_{28}_GBM): $a_1 = -2.8797$, $a_2 = -3.7072$, $b_1 = -3.8598$, $b_2 = -4.8411$ **cm** and (c) geometrical parameters (GEO_GBM): $a_1 = -2.7066$, $a_2 = -3.2681$, $b_1 = -3.7391$, $b_2 = -4.6112$ **cm**; (d) relative power error: (b)–(c). [Principal E-Plane in Fig. 1(b)].

TABLE II
SMA ABSOLUTE MAXIMAL RELATIVE POWER ERRORS (OPT_{28}_GBM—OTHER SIM_METHODS)

SIMULATION METHOD	MAX. ERROR: (OPT_{28}_GBM - SIM)		ACCURACY (COMMENTS)
	E- PLANE (FIG. 6)	H-PLANE (NO FIG)	
OPT_{04}_GBM	**0.0323**	**0.0428**	FAIR
OPT_{08}_GBM	**0.0259**	**0.0181**	GOOD
GEO_GBM	**0.0142**	**0.0323**	GOOD

100° and by under 5° only (quasi-plane wave) for the CSA. These phases differ considerably from the phase associated with conventional modeling (plane waves). On the other hand, Fig. 3(b) shows that the amplitude variations are fairly similar for the SMA and the CSA.

B. Studies of Experimental, Geometrical, and Optimization Results

1) Geometrical Studies: Invoking the geometrical (GEO_GBM) method, the source parametric values for the SMA were determined at 400 MHz ($\sigma = 1.09$ S/m, $\varepsilon_r = 77.14$) to be $a_1 = -2.7066$ cm, $a_2 = -3.2681$ cm, $b_1 = -3.73391$ cm, and $b_2 = -4.6112$ cm [1]. Similarly, the source parametric values for the CSA were determined at 450 MHz ($\sigma = 1.2$ S/m, $\varepsilon_r = 56$) to be $a_1 = -3.6492$ cm, $a_2 = -9.3403$ cm, $b_1 = -0.4140$ cm, and $b_2 = -6.6189$ cm [21]. Both sets of parametric values have been validated to give accurate simulation results compared with experimental results in Fig. 4 for the SMA applicator and in [1], [10], [21], [25], and [29].

2) Optimization Studies: Four (OPT_{04}_GBM), eight (OPT_{08}_GBM) and 28 (OPT_{28}_GBM) experimental values of normalized E-field in the paraxial region of the SMA applicator were selected from 100 measurements in the principal E- and H-planes and used in the GBM for parametric optimization. Table I(A) shows the optimized parametric values, the initially

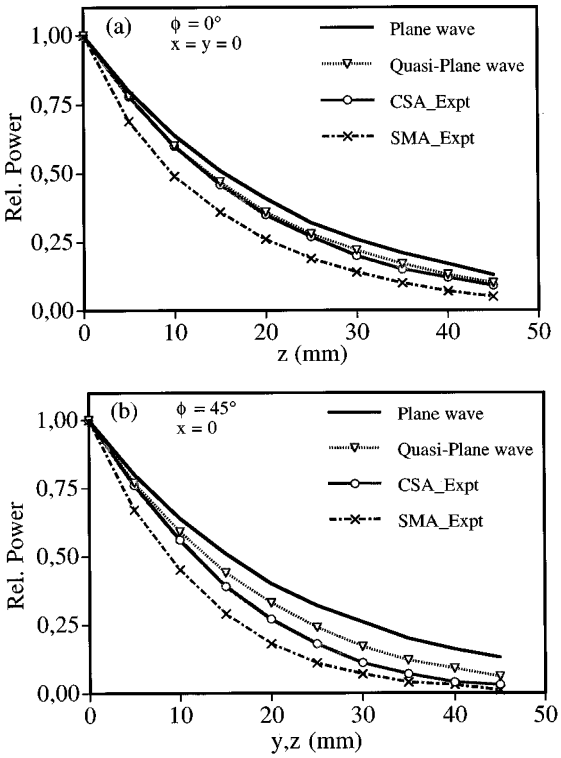

Fig. 7. Experimental (SMA_Expt at 400 MHz & CSA_Expt at 450 MHz) and simulated (Plane wave and Quasi-plane wave at 400 MHz) results in the principal E- and H-planes in Fig. 1(b) at $\phi = 0°$: (a) relative power and (b) error referenced to the global maximum (unity). [Simulation source parameters: quasi-plane wave set at 4 × (OPT_{28}_GBM) values, and plane wave set at 100 × (OPT_{28}_GBM) values].

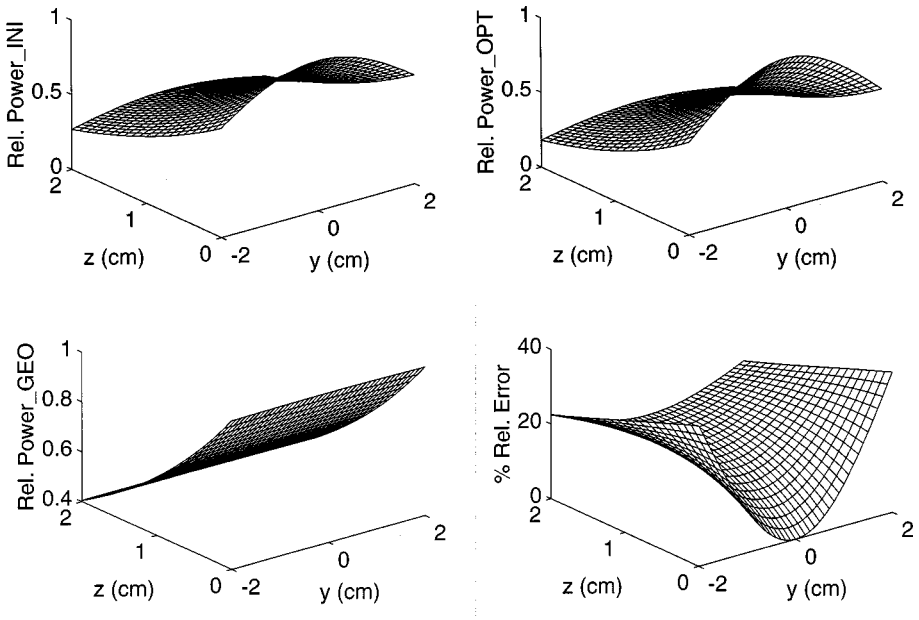

Fig. 8. EFS simulations at 400 MHz for the SMA and Plane-wave and 450 MHz for the CSA. (a) CSA parameters: $\boldsymbol{a_1} = -3.6492$, $\boldsymbol{a_2} = -9.3403$, $\boldsymbol{b_1} = -0.4140$, $\boldsymbol{b_2} = -6.6189$ **cm**, (b) SMA parameters: $\boldsymbol{a_1} = -2.8797$, $\boldsymbol{a_2} = -3.7072$, $\boldsymbol{b_1} = -3.8598$, $\boldsymbol{b_2} = -4.8411$ **cm** and (c) plane-wave parameters: 100 × (OPT$_{28}$_GBM) values; (d) SMA vs Plane-wave absolute % error (ref. global max). [Principal $\boldsymbol{E}$-Plane in Fig. 1(b)].

guessed values, and the GEO_GBM values. Finally, the parameters were used in (2) for simulations which are compared with experimental results in Figs. 4 and 5 and in Table I(B).

3) Comparison of Results: Compared with the experimental (Expt) results in Fig. 4(a)-(i), the accuracy of the OPT$_{28}$_GBM simulations is within 1% referenced to the global maximum (unity) and 2% for the GEO_GBM simulations [see Fig. 4(a)-(ii)]. Fig. 4(a)-(iii) depicts the local % error within the effective field size (EFS), defined in [30] as the area within the 50% SAR at a depth of 10 mm [z_d in Fig. 1(b)] from the surface of a plane, homogeneous, muscle-like phantom. Table I(B) shows the EFS local % errors to be within: i) 2.5% (OPT$_{04}$_GBM); ii) 3.8% (OPT$_{08}$_GBM); iii) 1.9% (OPT$_{28}$_GBM); and iv) 4.6% (GEO_GBM). These results must be taken in conjunction with those in Fig. 5 when considering the adequacy of the parameters. Fig. 4(b) shows the 2-D experimental and GBM-simulated results of relative power at $\phi = 45°$, in the principal $\boldsymbol{E}$-plane, where ϕ is shown in Fig. 1(b).

In Fig. 5 the experimental results are compared with the various simulations at depth $(z \geq 0)$, within the dominant paraxial region: $\phi = 0°$ and $x = y = 0$. The apparent errors between experimental and simulated results range 1–3% compared to the global maximum (unity). The best results are the OPT$_{28}$_GBM simulations (error within 1%) and the worst results are the OPT$_{04}$_GBM simulations (error within 3%). On the other hand, both the OPT$_{08}$_GBM and the GEO_GBM simulations are similar (error within 2%).

Fig. 6 shows relative (3-D) power in the principal $\boldsymbol{E}$-plane (similar results, not shown, were observed for the $\boldsymbol{H}$-plane), computed by means of the initial (INI), optimized (OPT$_{28}$) and geometrical (GEO) parameters. A plot of errors between the OPT$_{28}$_GBM and GEO_GBM results is also shown. Finally, the maximal relative power errors of OPT$_{04}$_GBM, OPT$_{08}$_GBM and GEO_GBM over the best simulation method (OPT$_{28}$_GBM) are shown in Table II. From these results, it is clear that the OPT$_{08}$_GBM and GEO_GBM are closer in accuracy to the OPT$_{28}$_GBM method than the OPT$_{04}$_GBM method.

C. Comparison of SMA, CSA, Quasi-Plane, and Plane-Wave Results

Figs. 7 and 8 depict results that highlight serious errors that would occur if the aperture field sources are not correctly modeled. The plane wave results were computed for source parameters set at 100 × (OPT$_{28}$_GBM parameters) and 4 × (OPT$_{28}$_GBM parameters) for the quasi-plane wave results [see Fig. 3(b)] for amplitude.

In Fig. 7(a) the relative power in the muscle-like phantom is shown for $z \geq 0$, $x = y = 0$ at $\phi = 0°$. It is seen that the experimental results for the CSA (CSA_Expt) and the quasi-plane wave results are similar. This is because the phase of the aperture field of the CSA [see Fig. 3(a)] is quasi-plane. On the other hand, the SMA deposits less power at depth ($z \geq 20$ mm) than the CSA. This makes the CSA a preferred choice for superficial hyperthermia [29] with other applicators [31]–[33] whose EFS are superior to that of the SMA. The plane wave relative power at depth is up to twice that of the SMA and about 25% more than the CSA value. At $\phi = 45°$ [Fig. 7(b)] the difference in the results at depth is worse by a factor of two, approximately.

Fig. 8 shows 3-D OPT_GBM results embracing the paraxial region for $0 \leq z \leq 2$ cm in the principal $\boldsymbol{E}$-plane. Similar results have been observed (not shown) for the principal $\boldsymbol{H}$-plane. Fig. 8(a) shows the CSA results, Fig. 8(b) the SMA results, and Fig. 8(c) the plane wave results. In Fig. 8(d) the difference between the SMA and the plane wave results is observed to be significant (over 20%) at depth. This difference would be, at least,

quadrupled for a four-applicator phased-array system used in superficial or deep tumor hyperthermia. This is borne out in [10, Ch. 4] where idealized sources (corresponding to plane waves) deposit twice as much focused SAR (50%) as the SMA sources (25%) in muscle, a difference of 100%.

IV. Conclusion

This paper has demonstrated how numerical modeling of field sources for electromagnetic hyperthermia can be improved by using an experimentally based model, the GBM. As an example, the EFIE has been linked to the GBM through the aperture and incident fields for numerical implementations using different algorithms. This link may apply to other field formulations such as the MFIE, etc.

This paper has presented the advantages and disadvantages of the two methods for implementing the GBM: 1) the geometrical method and 2) the optimization method. The former has been used successfully for several years, but is tedious to implement and relies on well-defined amplitude and phase profiles. On the other hand, the optimization method is new, accurate, and fast, requiring measured data of amplitude or power only in the paraxial region. This new method may be applied to more complex aperture antennas whose aperture fields are not suitable candidates for the geometrical method.

A study of the results showed that at least eight paraxial, experimental data values must be used in the optimization algorithm to give good results, comparable to the geometrical method (GEO_GBM) results. Improved OPT_GMB results may be achieved by using more than eight experimental data values (28 in this paper) from the principal $\boldsymbol{E}$- and $\boldsymbol{H}$-planes, close to and within the paraxial region. A minimum of 20 experimental data values are recommended.

A study of plane wave, SMA, and CSA power distributions has shown how serious modeling errors may be caused if the exact phases of the aperture fields are not modeled. These errors may be compounded when phased arrays are modeled by plane waves.

In a theoretical study (not included in this paper) it has been observed that when the optimization algorithm is applied to data corrupted by white noise set at 10% of the maximum, global pure data, it can still simulate the original, pure, data to within 4% of accuracy. This is a good result.

Finally, we conclude that the GBM is a viable model for characterizing applicators used in hyperthermia for cancer therapy. This can be achieved by executing the experimental procedures outlined in this paper to mimic exact cancer treatment setups. The source parameters determined by the model from the experimental data are unique characteristics of each applicator at the allocated frequency of operation. They can be used in numerical algorithms applied to the EFIE, the MFIE, etc. to prescribe practical aperture and incident fields, thus improving SAR simulations.

Acknowledgment

The author would like to thank Dr. S. W. R. Duym for his invaluable suggestions and input pertaining to the optimization procedure used in this paper.

References

[1] M. L. D. Lumori, J. B. Andersen, M. K. Gopal, and T. C. Cetas, "Gaussian beam representation of aperture fields in layered, lossy media: simulation and experiment," *IEEE Trans. Microwave Theory Tech.*, vol. 38, pp. 1623–1630, Nov. 1990.

[2] D. Livesay and K. M. Chen, "Electromagnetic fields induced inside arbitrarily shaped biological bodies," *IEEE Trans. Microwave Theory Tech.*, vol. 22, pp. 1273–1280, 1974.

[3] I. V. Lindell, *Methods for Electromagnetic Field Analysis*. Oxford, U.K.: Clarendon, 1992.

[4] G. A. Lovisolo, M. Adami, G. Arcangelli, A. Borrani, G. Calamai, A. Cividalli, and F. Mauro, "A multifrequency water-filled waveguide applicator: Thermal dosimetry *in vivo*," *IEEE Trans. Microwave Theory Tech.*, vol. MTT-32, pp. 893–896, 1984.

[5] J. R. Wait, "Focused heating in cylindrical targets, I," *IEEE Trans. Microwave Theory Tech.*, vol. MTT-33, pp. 647–649, July 1985.

[6] J. R. Wait and M. L. D. Lumori, "Focused heating in cylindrical targets, II," *IEEE Trans. Microwave Theory Tech.*, vol. MTT-34, pp. 357–359, Mar. 1986.

[7] J. R. Wait, "Analysis of the radiation leakage for a four-aperture phased array applicator in hyperthermia therapy," *IEEE Trans. Microwave Theory Tech.*, vol. MTT-34, pp. 531–541, Mar. 1986.

[8] M. L. D. Lumori, J. R. Wait, and T. C. Cetas, "Power deposition and focusing in a lossy cylinder by a concentric phased array," *Radio Sci.*, vol. 24, pp. 433–442, Apr. 1989.

[9] E. J. Gross, T. C. Cetas, P. R. Stauffer, R. L. Liu, and M. L. D. Lumori, "Experimental assessment of phased-array heating of neck tumours," *Int. J. Hyperthermia*, vol. 6, pp. 453–474, Feb. 1990.

[10] M. L. D. Lumori, "Microwave power deposition in bounded and inhomogeneous lossy media," Ph.D. dissertation, Dept. Elect. Comput. Eng., Univ. Arizona, Tucson, AZ, May 1988.

[11] H. Kogelnik, "On the propagation of Gaussian beams of light through lenslike media including those with loss or gain variation," *Appl. Opt.*, vol. 4, pp. 1562–1569, Dec. 1965.

[12] H. Kogelnik and T. Li, "Laser beams and resonators," *Proc. IEEE*, vol. 5, pp. 1550–1557, Oct. 1966.

[13] J. A. Arnaud and H. Kogelnik, "Gaussian light beams with general astigmatism," *Appl. Opt.*, vol. 8, pp. 1687–1693, Aug. 1969.

[14] G. A. Deschamps, "Gaussian beam as a bundle of complex rays," *Electron. Lett.*, vol. 7, no. 23, pp. 684–685, Nov. 1971.

[15] ——, "Ray techniques in electromagnetics," *Proc. IEEE*, vol. 60, pp. 1022–1035, Sept. 1975.

[16] A. Yariv, *Quantum Electronics*. New York, NY: Wiley, 1975.

[17] R. C. Weaver, W. Sache, and L. Niu, "Transient ultrasonic waves in a viscoelastic plate: Application to materials characterization," *J. Acoust. Soc. Amer.*, vol. 85, pp. 2262–2267, 1989.

[18] L. B. Felsen, J. M. Klosner, I. T. Lu, and Z. Grossfeld, "Source field modeling by self-consistent Gaussian beam superposition (two-dimensional," *J. Acoust. Soc. Amer.*, vol. 89, pp. 63–72, 1991.

[19] D. Zhou, L. Peirlinckx, M. L. D. Lumori, and L. Van Biesen, "Parametric modeling and estimation of ultrasonic fields using a system identification technique," *J. Acoust. Soc. Am.*, vol. 99, no. 3, pp. 1438–1445, March 1996.

[20] J. B. Andersen, "Electromagnetic power deposition: Inhomogeneous media, applicators and phased arrays," in *Physics and Technology of Hyperthermia*, S. B. Field and C. Franconi, Eds. Dordrecht, The Netherlands: Martinus Nijhoff, 1987, pp. 159–188.

[21] M. L. D. Lumori, J. W. Hand, M. K. Gopal, and T. C. Cetas, "Use of Gaussian beam model in predicting SAR distributions from current sheet applicators," *Phys. Med. Biol., (U.K.)*, vol. 35, pp. 387–397, Mar. 1990.

[22] A. Grace, *Optimization Toolbox User's Guide*. Natick, MA: The Math Works, 1990.

[23] P. M. van den Berg, A. T. De Hoop, A. Segal, and N. Praagman, "A computational model of the electromagnetic heating of biological tissue with application to hyperthermic cancer therapy," *IEEE Trans. Biomed. Eng.*, vol. 30, pp. 797–805, Dec. 1983.

[24] A. Stogryn, "Equations for calculating the dielectric constant of saline water," *IEEE Trans. Microwave Theory Tech.*, vol. MTT-19, pp. 733–736, Aug. 1971.

[25] M. K. Gopal, J. W. Hand, M. L. D. Lumori, S. Alkhairi, K. D. Paulsen, and T. C. Cetas, "Current sheet applicator arrays for superficial hyperthermia of chestwall lesions," *Int. J. Hyperthermia*, vol. 8, pp. 227–240, Feb. 1992.

[26] J. Bach Andersen, A. Baun, K. Harmark, L. Heinzi, P. Raskmark, and J. Overgaard, "A hyperthermia system using a new type of inductive applicator," *IEEE Trans. Biomed. Eng.*, vol. BME-31, pp. 21–27, 1984.

[27] R. H. Johnson, J. R. James, J. W. Hand, J. W. Hopewell, P. R. C. Dunlop, and R. J. Dickinson, "New low-profile applicators for local heating of tissues," *EEE Trans. Biomed. Eng.*, vol. BME-31, pp. 28–37, 1984.

[28] R. H. Johnson, A. W. Pierce, J. W. Hand, and J. R. James, "A new type of lightweight low-frequency electromagnetic hyperthermia applicator," *IEEE Trans. Microwave Theory Tech.*, vol. MTT-35, pp. 1317–1321, 1987.

[29] M. V. Prior, M. L. D. Lumori, J. W. Hand, G. Lamaitre, C. J. Schneider, and J. D. P. van Dijk, "The use of a current sheet applicator array for superficial hyperthermia: Incoherent versus coherent operation," *IEEE Trans. Biomed. Eng.*, vol. 42, pp. 694–698, July 1995.

[30] J. W. Hand, J. W. Lagendijk, J. Bach Andersen, and J. C. Bolomey, "Quality assurance guidelines for E.S.H.O. protocols," *Int. J. Hyperthermia*, vol. 5, pp. 421–428, 1989.

[31] P. J. M. Rietveld, M. L. D. Lumori, J. W. Hands, M. V. Prior, J. van der Zee, and G. C. van Rhoon, "Effectiveness of the Gaussian beam model in predicting SAR distributions from the lucite cone applicator," *Int. J. Hyperthermia*, vol. 14, pp. 293–308, 1998.

[32] P. J. M. Rietveld, M. L. D. Lumori, J. van der Zee, and G. C. van Rhoon, "Qualitative evaluation of 2×2 arrays of lucite cone applicators in flat layered phantoms using Gaussian-beam-predicted and thermographically measured SAR distributions," *Phys. Med. Biol. (U.K.)*, vol. 43, pp. 2207–2220, 1998.

[33] P. J. M. Rietveld, W. L. J. van Putten, J. van der Zee, and G. C. van Rhoon, "Comparison of the clinical effectiveness of the 433 MHz lucite cone applicator with that of a conventional waveguide applicator in applications of superficial hyperthermia," *Int. J. Radiation Oncology Biol. Phys.*, vol. 43, pp. 681–687, 1999.

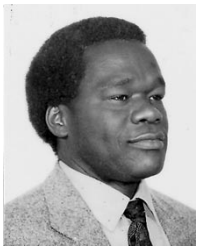

Mikaya L. D. Lumöri (M'89) was born in Yei, Southern Sudan, on June 18, 1950. He obtained the B.S.E.E. degree with honors in electronic engineering and the M.S.E.E. degree in communication engineering in 1971 and 1972, respectively, from the University of Manchester Institute of Science and Technology (UMIST), in England. In 1988 he obtained the Ph.D. degree in electrical engineering from the University of Arizona, Tucson.

From 1973 to 1977 he was a Faculty Member (Lecturer) in the Department of Electrical and Electronic Engineering at Makerere University, Kampala, Uganda. In July 1977 he became a Founding Member of the University of Juba in Southern Sudan, where he worked for several years as Associate Professor and Dean of Students. From 1988 to 1989 he was a Faculty Research Associate at the University of Arizona Health Sciences Center, Tucson. From 1989 to 1990 he was a Research Scientist with the Medical Research Council Cyclotron Unit, Hammersmith Hospital, London, England. Subsequently, he worked as a Research Fellow (1990–1991) in the Department of Electrical and Electronic Engineering, University College London, England. In December 1991 he joined the Department of Electrical Engineering, Vrije Universiteit Brussel, in Brussels Belgium (VUB), where he taught courses at Vesalius College VUB for over eight years as an Associate Professor. Currently has is a tenure-track Associate Professor of electrical engineering at the University of San Diego, San Diego, CA. His research interests include Gaussian beam modeling of electromagnetic field sources, applied electromagnetics, electromagnetic hyperthermia, ultrasonics (underwater acoustics and medical applications), and parametric identification in systems.